Single-Particle Tracking and Trajectory Analysis of Fluorescent Nanodiamonds in Cell-Free Environment and Live Cells

Sigaeva, Alina; Hochstetter, Axel; Bouyim, Sighom; Chipaux, Mayeul; Stejfova, Miroslava; Cigler, Petr; Schirhagl, Romana

Published in:
Small

DOI:
10.1002/smll.202201395

NANO · MICRO small
www.small-journal.com

Single-Particle Tracking and Trajectory Analysis of Fluorescent Nanodiamonds in Cell-Free Environment and Live Cells

*Alina Sigaeva, Axel Hochstetter, Sighom Bouyim, Mayeul Chipaux, Miroslava Stejfova, Petr Cigler, and Romana Schirhagl**

Diamond magnetometry can provide new insights on the production of free radicals inside live cells due to its high sensitivity and spatial resolution. However, the measurements often lack intracellular context for the recorded signal. In this paper, the possible use of single-particle tracking and trajectory analysis of fluorescent nanodiamonds (FNDs) to bridge that gap is explored. It starts with simulating a set of different possible scenarios of a particle's movement, reflecting different modes of motion, degrees of confinement, as well as shapes and sizes of that confinement. Then, the insights from the analysis of the simulated trajectories are applied to describe the movement of FNDs in glycerol solutions. It is shown that the measurements are in good agreement with the previously reported findings and that trajectory analysis yields meaningful results, when FNDs are tracked in a simple environment. Then the much more complex situation of FNDs moving inside a live cell is focused. The behavior of the particles after different incubation times is analyzed, and the possible intracellular localization of FNDs is deducted from their trajectories. Finally, this approach is combined with long-term magnetometry methods to obtain maps of the spin relaxation dynamics (or T1) in live cells, as FNDs move through the cytosol.

1. Introduction

Diamond magnetometry is a promising technique, applied in materials science,[1,2] spin electronics,[3] quantum sensing, and, lately, for detecting magnetic field fluctuations in chemical[4–6] and biological samples,[7] including individual living cells.[8,9] For intracellular measurements, fluorescent diamond nanoparticles (Fluorescent nanodiamonds [FNDs]) can be used. FNDs, internalized by a cell, offer extremely high spatial resolution (on the order of 10–20 nm). However, making full use of this resolution is currently difficult, because the recorded signals generally lack intracellular context. While the behavior and the fate of FNDs in cells and living organisms has been investigated for over a decade[10,11] most of the studies offer a generalized, statistical perspective on where one can expect to find FNDs. The intracellular fate (i.e., whether it is retained in the intracellular vesicles, undergoes the endosomal escape, is targeted toward a specific organelle) of an individual particle in each particular measurement is largely unknown and can only be established by post-measurement correlative microscopy. However, this approach is extremely low-throughput, and only provides the information on the final destination of the FND, not the events that have occurred during the measurement. This poses a particular challenge in case of long-term measurements, spanning hours, during which the signal is continuously recorded from the particle travelling through the cell. One way to circumvent this problem is to specifically target FNDs to a location of interest.[8]

One approach to solve this problem is analyzing the trajectory of the particle. Mean squared displacement (MSD) analysis is widely used for this. Previous studies have attempted to analyze the intracellular behavior of FNDs through MSD analysis. One of the notable pioneering works has been performed by Simpson and co-authors, who used the FNDs injected in the fruit fly embryos to assess the viscosity of the intracellular environment, as well as the presence of active transport of the cellular components in different parts of the embryos.[12] In another elegant work, published by Liu and co-authors, FNDs conjugated with transforming growth factor (TGF) were used as labels for the TGF receptor on the surface of live cells.[13] Single-particle

A. Sigaeva, S. Bouyim, R. Schirhagl
University Medical Center Groningen
Groningen University
Antonius Deusinglaan 1, Groningen 9713AV, The Netherlands
E-mail: romana.schirhagl@gmail.com

A. Hochstetter
Research & Development
Life on a Chip e.K.
Brunnenaecker 5, 73571 Goeggingen, Germany

M. Chipaux
Institute of Physics
Life on Chip e.K.
École Polytechnique Fédérale de Lausanne (EPFL)
Lausanne CH-1015, Switzerland

M. Stejfova, P. Cigler
Institute of Organic Chemistry and Biochemistry of the Czech Academy of Sciences
Flemingovo nam. 2, Prague 166 10, Czech Republic

The ORCID identification number(s) for the author(s) of this article can be found under https://doi.org/10.1002/smll.202201395.

DOI: 10.1002/smll.202201395

Table 1. Summary of FND tracking inside living cells.

Reference	FND size [hydrodynamic diameter]	FND surface coating	Cell type	Delivery method	Total tracking time	Time between two consecutive positions [s]	Calculated diffusion coefficient [$\times 10^{-4}$ μm^2 s^{-1}]	Number of trajectories
[15]	52 nm	*Cowpea chlorotic mottle virus* capsid proteins	HeLa (human, epithelial)	Endocytosis	43 min (1 trajectory), 7 min (2 trajectories)	4.96	2.09	3
[16]	30–60 nm	Cationic, PEGylated denatured human serum albumin	bEnd.3 (mouse, neuronal)	Endocytosis	45 min	–	–	1
[17]	110–120 nm	Hyperbranched polyglycerol, alkyne-modified	HeLa (human, epithelial), HWF (human, fibroblasts)	n/a, FNDs were used to label cell surface molecules	5 min	0.10	41 (on the cell membrane)	≈2000
[14]	30 nm	–	Mouse hippocampal neurons	Endocytosis	from 2 min to 1 h	0.05	16	≈2000 (under multiple experimental conditions)
[18]	30 nm	Hyperbranched polyglycerol, ampicillin-modified	HEK293 (human embryonic kidney)	n/a, FNDs were used to label cell surface molecules	8 s	0.02	5000	15
[13]	40 nm	TGF, bovine serum albumin	HCC827 cells (human, epithelial)	Endocytosis	5 s	0.05	100 (treated as immobile) 2000 (confined/ anomalous diffusion) 30 000 (free diffusion)	775
[19]	100 nm	Bovine serum albumin	HEK293T (human embryonic kidney)	Endocytosis	2 min	0.50	20 (in the cytoplasm) 80 (in the tunneling nanotubes)	50
[12]	131 nm	–	*Drosophila melanogaster* (fruit fly) embryonic cells	Microinjection	5 s	0.20	60 (in the blastoderm cells) 650 (in the periplasm between the nuclei and the yolk)	73
[20]	35 nm	Polyethylene glycol, folic acid	HeLa (human, epithelial)	Endocytosis	6.2 min	0.10	20	1
[21]	35 nm	–	HeLa (human, epithelial)	Endocytosis	3.3 min	0.10	31	1
[22]	35 nm	–	HeLa (human, epithelial)	Endocytosis	14 s	0.14	–	1

tracking of FNDs bound to the receptors allowed the authors to study the real-time dynamics of the receptors and the way it changes during the transmembrane signaling. Intracellular tracking of FNDs was used by Haziza and co-authors as a sensitive tool to spot the slight abnormalities in the intraneuronal transport, characteristic for a wide range of neurological conditions, including Alzheimer's disease.[14] This study highlights the potential of single-particle tracking of FNDs for both fundamental and clinical research. **Table 1** summarizes the papers on FND tracking in live cells, published over the last 15 years.

The results yielded by single-particle tracking can vary a lot due to the sample size, different cells, different particle sizes and shapes, different processes studied, and different techniques used to record the trajectories. In this study, we attempt to perform a step-by-step analysis of the behavior of FNDs. We start with simulating different kinds of trajectories that can, in principle, be exhibited by an internalized nanoparticle, and analyzing those. We then apply these results to the analysis and interpretation of the behavior of FNDs in glycerol solutions. Last, we use the obtained knowledge to assess the differences in movement of FNDs in living cells at different stages of the uptake (2 or 24 h of incubation). We also show that trajectory analysis can be combined with nanodiamond magnetometry measurements to provide additional information on the context of recorded T1 values.

2. Results and Discussion

2.1. Simulated Trajectories

The main tool we used to analyze the trajectories of the FNDs in this chapter is the MSDs. **Figure 1** illustrates three main

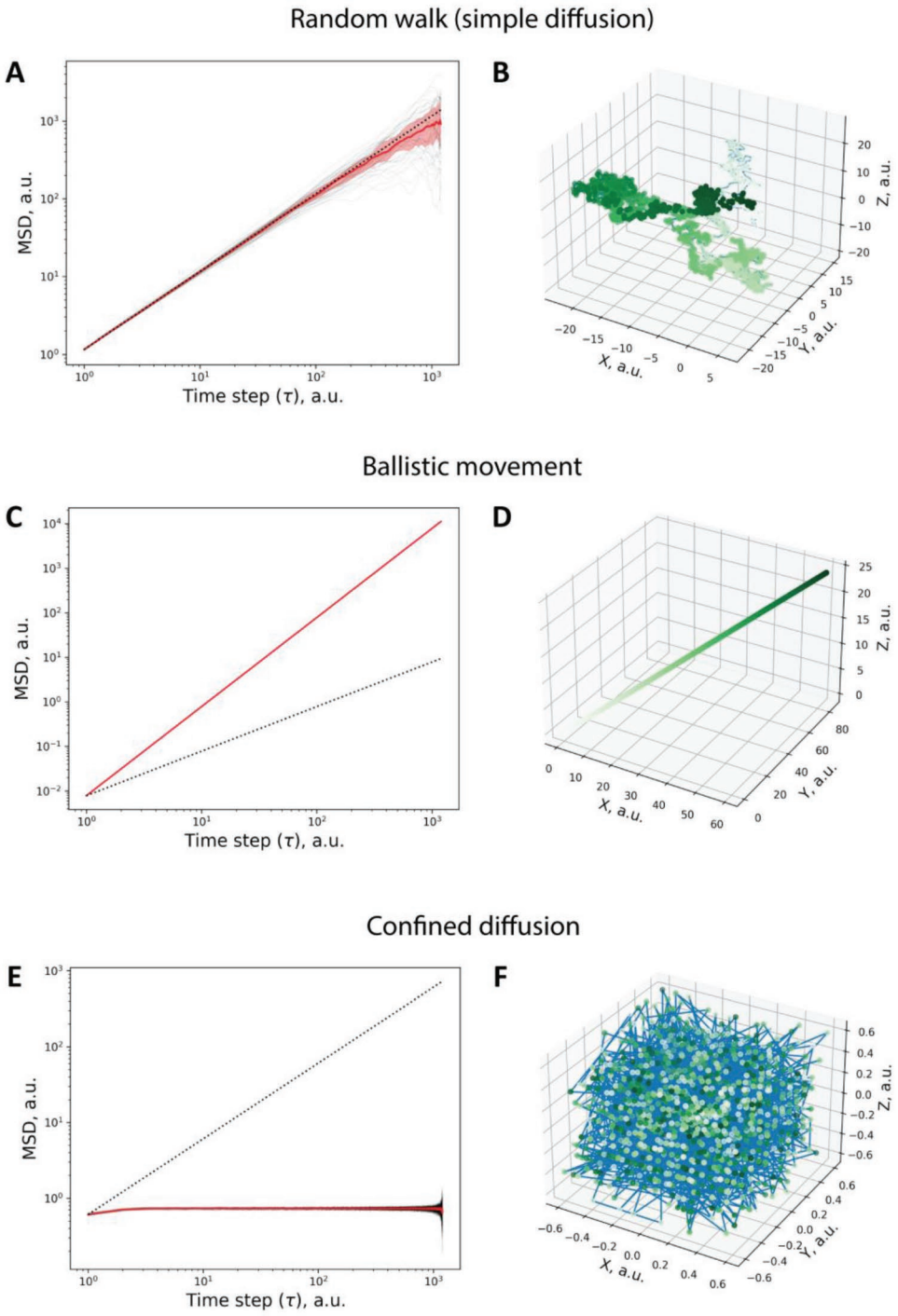

Figure 1. Three basic types of particle movement. On the left side (A,C,E) are the mean squared displacements (MSDs) versus the time interval between two positions. Each figure shows 50 individual MSDs of simulated trajectories (grey lines) and the median of all MSDs of this simulation set as a bold red line. The red shading represents the interquartile range. The dotted black line depicts a slope of 1, indicating ideal random movement. On the right side (B,D,F) is a randomly chosen trajectory from that set of simulations.

types of particle movements (random walk/simple diffusion, ballistic motion, and confined diffusion) and the corresponding MSDs. We now state a few general characteristics of MSDs and how they correspond to the trajectories that the MSDs have been calculated from. First, MSDs are plotted in a log–log scale, with the MSD (of a particle moving away from its origin) on the *Y*-axis. On the *X*-axis, we plot the time interval. This means that the first point in the graph represents the distance travelled between two positions (squared to avoid negative values)—while taking one single step. This is the average of

displacement occurring between any two positions, so it is averaged over the entire trajectory. On the one hand this can be seen as the average speed ($v = s/t = r^2(1)$), where v is the velocity, s the distance traveled, t the time, and $r^2(1)$ the squared displacement at step size 1. On the other hand, one can also calculate the diffusion coefficient (D) from it, according to $r^2(\tau) = 2n \cdot \tau^\alpha \cdot D$, with $r^2(\tau)$ being the MSD during the interval τ, n being the number of dimensions in which the trajectory is travelling, τ^α being the time interval, and the slope α. Subsequently, the next point on the graph, is the distance that the particle has covered between two consecutive steps (as in, between three positions on the trajectory), followed by the displacement during three steps, and so on.

The last point of the curve is how much the particle has travelled along the entire trajectory. For this, there is only one single value, as we have only one full trajectory. The second to last point on the graph, however, is an average of two values. Hence, with increasing step size, the statistical weight decreases and thus the signal-to-noise ratio rises. That is why MSDs are generally noisy toward the end.

The slope α in the MSD graph reflects the mode of motion (Figure 1). A slope of $\alpha = 1$ indicates ideal random movement, $\alpha = 2$ reflects ballistic motion (as in, active/consistent propulsion along the same direction), and $\alpha = 0$ is for confined particles.

The MSDs of confined particles end in a plateau, which indicates that the particles have been to all parts of the available space. And since the MSD is a measure of the space a particle has explored, it has reached its maximum—no matter how long we observe the particle (how large the time step τ is), it will not be able to move further away. The corresponding trajectories fill the confinement entirely and allow one to see the size and shape of the confinement itself. The size of the confinement can be calculated from the Y-value of the MSD plateau. By taking the square root of that Y-value, we arrive at the radius of the confinement. At the end, the MSD will show fluctuations, depending on how close (below) or far (on top of the plateau) the end point is from the start of the trajectory.

It is important to note that within every confinement, random motion takes place, as long as the particles are smaller than the confinement. It means that, theoretically, every MSD curve for a confined trajectory should start with a slope of $\alpha = 1$, and this part can be used to calculate the diffusion constant D. However, small particles—like FNDs—generally move much faster than their positions are recorded. In this case, one might observe the MSD curve that starts directly with a plateau or a slope of $\alpha < 1$. The size of D can then still be calculated from the value of MSD($\tau(1)$), but it will be underestimated, and for correct calculations, τ would need to be shorter (meaning higher acquisition rate for the particle's position). On the other side, to properly detect the plateaus in the MSDs, it is necessary to record the trajectories for a long enough time.

Figure 1A,B shows truly random motion of a particle with a variety of step sizes in all three dimensions. Each step is independent of the one before both in size and direction. The MSD of such a trajectory depict a slope of $\alpha = 1$, all along the graph. Toward the end, the signal-to-noise ratio drops, as fewer and fewer data points are available, and thus the slope deviates from the ideal form. Ballistic motion (Figure 1C,D) results in a very straight-line trajectory and a straight MSD curve with a slope of $\alpha = 2$. In case of a particle being confined within a cube with a side of 1.2 arbitrary units (a.u.), (Figure 1E,F), the MSDs end in a plateau, while the trajectory shows the shape and size of the confinement.

The parameters derived from the trajectories and MSD curves are summarized in Table S1, Supporting Information. The total displacement and the volume explored by the particle are clearly different between three modes of movement. It is worth noting that ballistic movement results in a larger increase in the total distance travelled by the particle, but the explored volume does not increase as much. As the particle moves ballistically in one direction, its displacement in the plane perpendicular to the direction of ballistic movement is equal to zero. The resulting trajectory looks like a narrow tube (or a line), and its volume is relatively small. At the same time, an unconfined particle has the freedom to move in all three dimensions, thus exploring a relatively large volume. As expected, a confined particle would have a much smaller volume available to it. Since this volume is relatively small, as compared to the step of the particle (the particle's displacement between two consecutive positions on the trajectory), it will affect the MSD curve (it starts with a slope of $\alpha < 1$). The resulting diffusion coefficient will be underestimated (thus being lower than that in case of the unconfined particle).

As our simulations show, the size of the confinement, its own movement, and the shape of the confinement all have pronounced effects on the shape of MSD curves, the calculated diffusion coefficients, total displacements of the particle, and the total volume explored by the particle. The results of the simulations, as well as the analysis of the resulting trajectories, are summarized in Supporting Information.

With the transition to real data, however, one needs to take into account certain factors that can affect the results. The static and dynamic errors that occur in experimental particle tracking (i.e., not recording every infinitely small/fast displacement [= finite localization error], limit in resolution due to camera pixel pitch and shutter speed) are discussed more in depth by Savin and Doyle,[23] and the difference of actual position versus recorded position and its impact on the diffusion constant D are detailed on in the paper by Michalet.[24] In our experiments, these effects show themselves during the tracking of the particles (Figure S17, Supporting Information). The tracking is done by first fitting the brightness of an X–Y-image with a 2D Gaussian distribution and then finding the brightness maximum in an Z-scan. Both steps limit our resolution and introduce a finite localization error. In the X–Y-plane, our resolution is limited to the confidence interval of our Gaussian fit (0.11 µm in X and Y). In Z, we are taking eight scans of a thickness of 2 µm. The error can be reasonably assumed to be +/−1 layer, hence 0.25 µm. The effect of the different lateral and depth resolution can also be seen in **Figure 2**. This led to us excluding the Z-axis data in the later analysis.

As for the temporal resolution, we recorded the images at a frequency of ≈1 Hz and are thus slower than most measurements that do not study biological samples. Naturally, having a longer lag time (i.e., lower frequency) between two successive points in a trajectory has an impact on the MSD derived from that trajectory: the faster and shorter displacements of

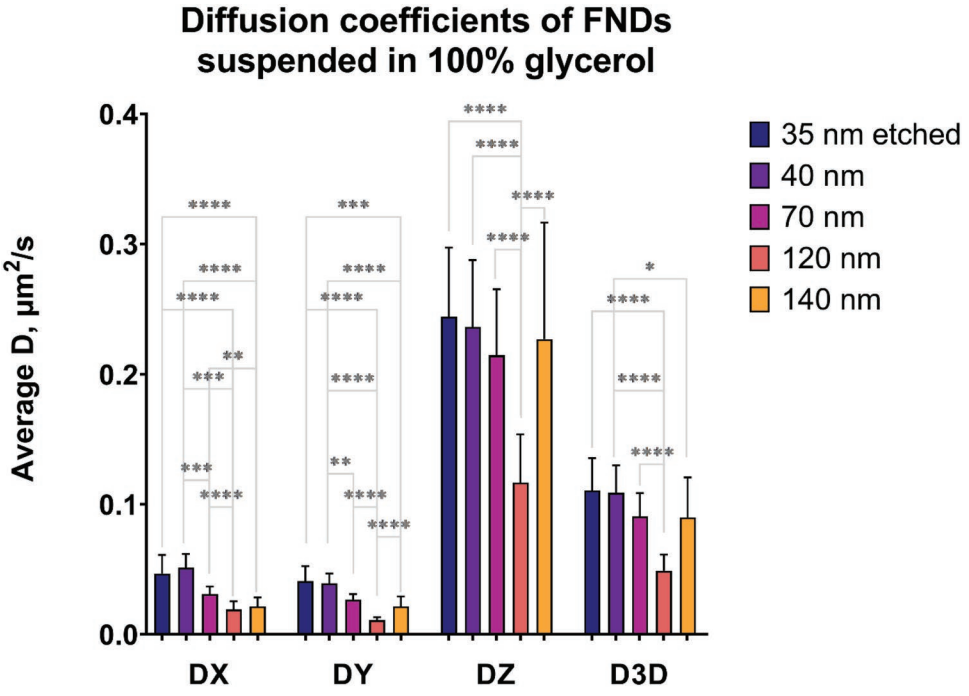

Figure 2. Diffusion coefficients of FNDs suspended in 100% glycerol. The results are shown as mean ± standard deviation. The number of trajectories analyzed in each group is: 35 nm etched: 14, 40 nm: 40, 70 nm: 37, 120 nm: 40, 140 nm: 40. The asterisks indicate the statistical significance of the differences between groups, measured with Kruskal–Wallis test and Dunn's post-hoc multiple comparisons test. *: $p < 0.05$, **: $p < 0.01$, ***: $p < 0.001$, ****: $p < 0.0001$.

the tracked particle (situated in the lower-left quadrant of the MSD) are missing. For confined particles this might mean that the points of the trajectories are far enough apart that the confinement already influences the particle's smallest recorded steps. This is a situation we will often encounter when probing biological samples with FNDs or similar nanoscale probes. We show and discuss the impacts of different confinement shapes and sizes on both trajectories and MSD curves in detail throughout the Supporting Information. The presence of a confinement generally leads to a lower diffusion coefficient D. To compensate for this, the slope α is introduced in calculating D as $D = \frac{r^2(\tau)}{2n \cdot \tau^\alpha}$, which is derived from the formula $r^2(\tau) = 2n \cdot \tau^\alpha \cdot D$. Obtaining the slope α from a measured trajectory comes with several caveats, depending on the measurement and what is known about it and has been discussed in depth already.[23,24,26] Other parameters derived from the trajectory such as total displacement of the particle or total volume explored might also be useful in differentiating the nature of the confinement.

While we generally discuss MSD from the point of view of normal diffusion, we intentionally insert disruptions into certain parts of the trajectories such as confinement or linear motion replacing the pure diffusion. These disruptions cause well-established statistical effects in the MSDs. Both the disruptions and the effects they have on the MSD are discussed in the Supporting Information.

An often encountered feature in not purely diffusive motion is loss of ergodicity (ergodicity: here, the property, that the tracked particle can/will reach all possible positions of its confinement): As Metzler et al. demonstrated in 2014[25] and Kepten et al. discussed in 2015,[26] a particle that exhibits not only diffusive behavior can cause a "weak break in ergodicity," resulting in the MSD not scaling with the time step τ. A particle freely diffusing in water/glycerol within a confined volume can be assumed to be ergodic. Confining that particle within a moving cell or with different regions of viscosity will break the ergodicity of the system, which also shows in the MSD and how it scales with the time step τ. An in-depth discussion on the different scalings can be found in the paper by Metzler et al.,[25] while Kepten et al.[26] provide a guide on how to fit them. An additional analytic tool, the velocity auto-correlation function, and its representation of different particle trajectories and modes is given in the papers by Weber et al.[27] and Backlund et al.[28]

These are suggestions for interested readers and would be beyond the scope of this study. The exact nature of the movement of particles within a biological sample is often still unknown, and thus a more complicated, yet appropriate fit can be impossible to choose. This publication is intended as a general guide for the researchers aiming to combine trajectory analysis and NV-based sensing. Thus, we mostly focus on the diffusion coefficient and basic shape description of the MSD curves without full in-depth analysis of the trajectories.

2.2. FND Trajectories in Glycerol

In this section, we analyze MSDs that were recorded from FNDs of different sizes, suspended in glycerol solutions, and compare them to the simulated MSDs to analyze the movement of the

particles. The first step was to assess the drift of the experimental setup, for which we used the trajectories recorded from dry samples with 120 nm FNDs. The results and discussion are presented in the Supporting Information section "Drift correction." Briefly, we observed drift along one of the axes in one of our setups. A total of 26 independent measurements were taken on different days and times of the day (ranging from 10 am to 5 pm). As we couldn't measure the drift within the setup, during the measurements, the drift was calculated on the same setup without any cells or fluid. The speed of the drift, as calculated from the linear fit of the displacement of the particles, amounted to 0.021 μm min^{-1}. This value was further subtracted from the trajectories to correct for the drift.

Since this is representing a typical drift and not the actual drift, this has to be taken into account when reproducing these experiments and discussing the results. The actual drift during the measurement can be influenced by the environmental conditions (most notably, temperature fluctuations) and the mechanical vibrations inevitably present in the building (for example, due to the foot traffic).

Another issue to take into account is the localization precision. As mentioned previously, finding the apparent position of the particle relies on fitting the experimental data of the fluorescence intensity. The digital nature of the data means that this fitting is done on a limited number of data points (one cannot represent the image with an infinite number of pixels). We estimated the uncertainty of the fitting from 100 images of a diffusing particle. Each image covered the area of 2 × 2 μm and consisted of 10 × 10 pixels. We found that the uncertainty of the Gaussian fit is 0.11 ± 0.07 μm, which translates to an average squared displacement of 0.012 μm^2 and a variance of 0.0045 μm^2 (Figure S17, Supporting Information).

Even if there is no drift and the fitting is perfect, the optical system itself introduces a certain localization error, since the size of our particles is generally below the diffraction limit. As a result, the apparent displacement of the immobilized particle is not equal to zero. The detected position of the immobilized particle fluctuates around the point of origin (Figure S15B, Supporting Information). To estimate the impact of this kind of the measurement noise, we assessed the MSD at the shortest lag time in *XY* plane from the trajectories of immobilized FNDs (Figure S18, Supporting Information). The immobilized particles show an apparent MSD of 0.0308 ± 0.0070 μm^2, which is one to two orders of magnitude less than that of the diffusing FNDs. Since both the finite localization error and the localization error of the optical system are negligible, we do not expect them to affect our results.

Interestingly, almost none of the curves in **Figure 3** can be described as straight lines, which would correspond to simple, unconfined diffusion. In most cases, FNDs moving in glycerol solutions show varying degrees of confinement. Individual trajectories vary a lot, emphasizing the need for thorough analysis of the particle's movement even in simple environments. While for the following cases shown in Figure 3A–G, the α is less than 1 for shorter times, and the lower slope could partially be explained by having an acquisition time too long to record every infinitely small displacement (finite localization error), and the overall shape and the corresponding trajectories (see **Figure 4**) indicate other effects that we mention below.

FNDs moving in 100% glycerol exhibit additional curvature of the MSD plots (Figure 3A,C,E), which is less pronounced in case of the 40 nm FNDs (Figure 3G). This behavior of MSDs resembles two scenarios from the simulations. The first one is moving confinement, which also has a plateau at low τ, reflecting the size of the confinement, and an upward curve with $\alpha > 1$ at high τ, corresponding to the ballistic movement of the container (Figure S2, Supporting Information). The second scenario is confinement that is only present on certain parts of the trajectory (Figures S4E and S5C,E, Supporting Information), which results in a curved MSD plot, deviating from the straight line at the middle. The confinement (if present) must be relatively large, as there is no well-defined plateau, and the particle must have relatively large periods of diffusing freely, as the MSD curves do not exhibit the characteristic scythe-like feature (Figures S4 and S6, Supporting Information). One of the possible scenarios is the particle moving between the domains of the sample, diffusing freely within the boundaries of one domain, then "jumping" to the neighboring one. This is the behavior observed in the 3D trajectories of FNDs (Figure 4).

40 nm FNDs exhibit the behavior closest to free diffusion (Figure 3G), with the exception of the highly confined trajectory, which is shown in Figure 4D. In this case, the particle seems to be trapped within the sample or have fallen to the very bottom and is not able to diffuse freely within the solution.

100% glycerol is, in fact, a sample that contains a certain percentage of water—from the FND stock solution (3 μL mL^{-1}) and from the atmosphere, as pure glycerol is highly hygroscopic. It has recently been shown that microscopic pockets of different glycerol concentration (and viscosity) can form during the mixing of glycerol and water.[29] The persistence of these domains can be explained by comparatively slow movement of glycerol molecules between distinct domains of more water-rich regions.[30] Nakagawa and Oyama concluded that, due to difference in H-bond strength, water in water–glycerol mixtures can move faster than in bulk.[31] These super-fast water molecules would play the diffusive part, which in turn means that pockets of high-density glycerol can remain in bulk for long times, generating the pockets we encounter. In experiments, where water–glycerol mixtures were frozen, water was freezing on the interface of glycerol-rich domains,[30,32] further demonstrating the existence of distinct domains of different viscosities in water–glycerol solutions.[30]

Such areas of varying local viscosity might lead to the particles being "confined" within a bubble of lower viscosity, as the stock solution of FNDs is mixed with the sample. This heterogeneity is less pronounced, when the viscosities of the two mixed solutions are closer to each other (e.g., if pure water is mixed with 50% glycerol), so we would expect to see less of this behavior in less concentrated glycerol solutions. Indeed, the MSD curves from the 75% glycerol samples (Figure 3B,D,F,H) are generally closer to those for simple diffusion.

Another report of the nanoparticles switching between a random walk and "jumps" during their diffusion can be found in the publication by Zheng and coauthors.[33] In that case, small (5–15 nm) spherical and rod-shaped golden nanoparticles were tracked with very high precision for ≈4 min in a film of water–glycerol mixture. The authors report on the complex trajectories, with noticeable transition between "swarms" of small

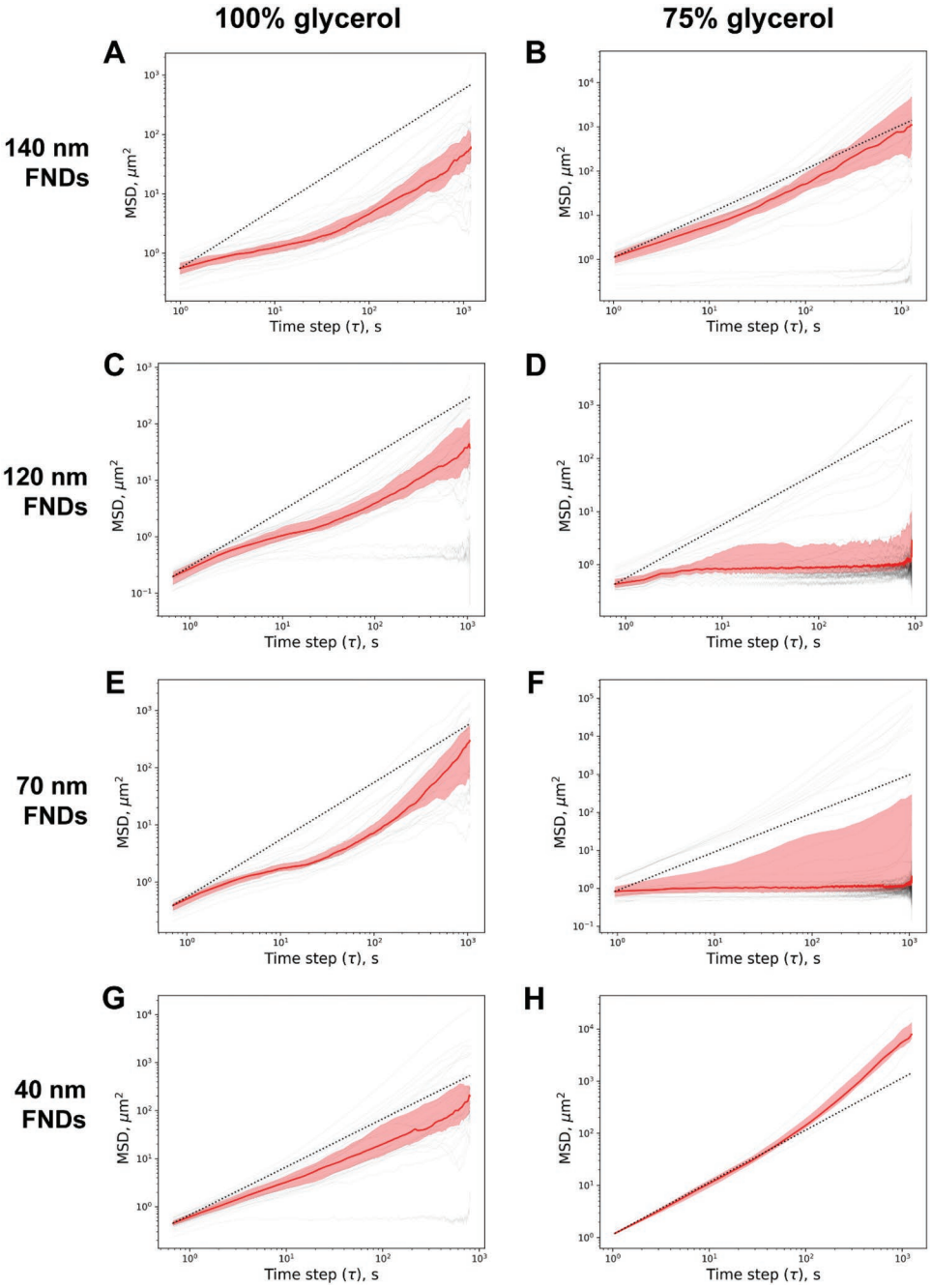

Figure 3. MSD curves of the FND trajectories in glycerol solutions. The left column A,C,E,G) corresponds to the particles in pure glycerol. The right column B,D,F,H) shows MSD curves, coming from the trajectories in 75% glycerol solution in water (by weight). Each row corresponds to the particles of a certain size (hydrodynamic diameter), from 140 to 40 nm. Each figure shows individual MSDs of trajectories as grey lines and the median of all MSDs under the given conditions is set as a bold red line. The dotted black line depicts a slope of 1, indicating ideal random movement. The shaded red region shows the interquartile range of MSDs. The number of the trajectories shown in each panel is: A: 40, B: 40, C: 40, D: 40, E: 37, F: 40, G: 40, H: 4 (the smallest FNDs diffusing in 75% glycerol are almost impossible to track under the limitations of our spatial and temporal resolution).

steps and rare "jumps" that cover a significantly larger distance. Interestingly, this behavior was more pronounced in larger nanoparticles. These "jumps" were not caused by the drying up of the film and were not correlated between the neighboring particles. The authors come to the conclusion that the "jumps" represent the rolling of the particles which can be caused by the local convective flow. However, it is worth noting that these effects were observed at a smaller scale and in a rather different experimental model.

In most cases for 75% glycerol samples, we observe two subsets of MSD curves. One is close to simple diffusion, occasionally with additional ballistic movement; the other one is highly confined, with particles almost not moving. The first subset corresponds to FNDs floating in the glycerol, while the second one

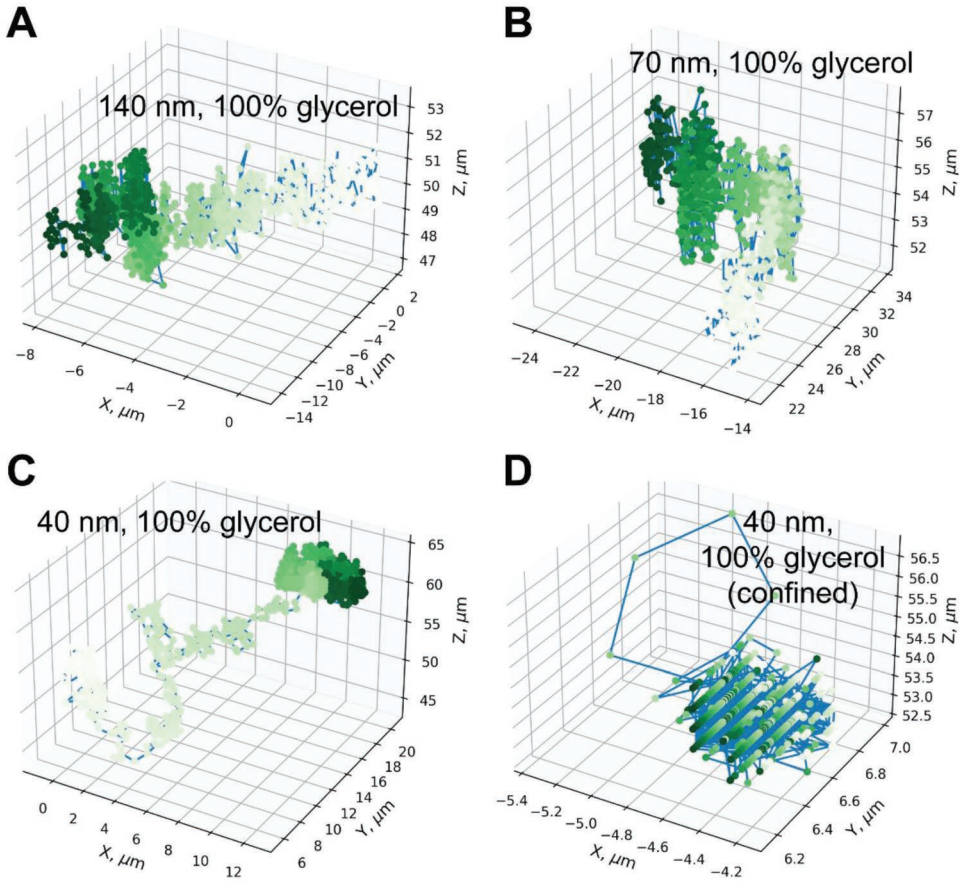

Figure 4. Examples of FND trajectories in 100% glycerol for 140 nm (A), 70 nm (B) and 40 nm (C,D) particle.

likely results from the trajectories of FNDs at the bottom of the sample, which do not diffuse as easily. As 75% glycerol is less viscous and less dense, the buoyant force acting on the particles will be smaller, so we expect to see more of them falling to the bottom over the course of the experiment. 40 nm FNDs show clear combination of random diffusion and ballistic movement (Figure 3H; compare to Figure S1C, Supporting Information). The ballistic movement that we observe in most of the samples might be caused by several factors: the free fall of the particles, the drift of the sample, and the flow of glycerol that might happen due to the local heating of the sample. However, it is clear from the MSD curves that the ballistic motion is relatively slow, as compared to the random walk of the particles.

We then used the calculated MSDs to derive the diffusion coefficients for each of the experimental groups in each of the dimensions (separately in *X*, *Y*, And *Z*), as well as the overall diffusion coefficient. The results are summarized in Figure 2.

Smaller FNDs consistently exhibit higher diffusion coefficients, which is to be expected, as, according to the Stokes–Einstein equation, D is inversely proportional to the hydrodynamic radius of the particle ($D = \frac{k_B T}{6\pi\eta r}$, with diffusion coefficient D, the Boltzmann constant k_B, the absolute temperature T, the viscosity η, and the hydrodynamic radius r of the diffusing particle). In *X*, the diffusion coefficient of 70 nm particles was roughly two times smaller than that of 38- and 40-nm ones, while being roughly 1.5 times larger than that of 120 nm particles. Notably, we could not observe significant differences in the diffusion coefficient of 120 and 140 nm FNDs. As reported by manufacturer, these particles display a range of sizes, with size distributions showing substantial overlap.

Figure 2 also highlights certain limitations of our experimental setup. Diffusion coefficient in *Z* is consistently larger than that in *X* or *Y*, by roughly an order of magnitude. This discrepancy likely stems from the worse resolution of the confocal microscope in *Z*. It means that the vertical position of the particle cannot be identified as precisely, and the smallest detectable displacement of the particle in *Z* will be larger than that in *XY* plane. This will lead to the particle "jumping" along the vertical axis, resulting in an overestimated *D*. To avoid the errors introduced by this limitation, we used either the diffusion coefficient in *X* (*DX*) or the diffusion coefficient in two dimensions, *X* and *Y* (*DXY*) for future analysis and calculations.

The Stokes–Einstein equation referenced earlier can be used to estimate the theoretical diffusion coefficient for the particle of a given size in the solution of a given viscosity. The comparison of the theoretical diffusion coefficients for FNDs of different size with the experimentally recorded ones is given in Table S2, Supporting Information. For 100% glycerol, the diffusion coefficients are substantially higher than theoretical ones in all experimental groups. This can be explained by glycerol being, in fact, a mixture of glycerol and water. At

Table 2. Viscosities (η) of glycerol solutions and corresponding glycerol concentrations, as estimated from the diffusion coefficients of FNDs along the *X*-axis.

FND hydrodynamic diameter [TEM for round particles]	100% glycerol [theoretical η = 1.4138 Pa s]		75% glycerol [theoretical η = 0.035 1 Pa s]	
	Calculated η [Pa s]	Calculated glycerol concentration [% by mass]	Calculated η [Pa s]	Calculated glycerol concentration [% by mass]
38 nm round	0.2622	91%	–	–
40 nm	0.2091	89%	0.0545	79%
70 nm	0.1983	89%	0.4813	94%
120 nm	0.1869	89%	0.0533	79%
140 nm	0.1426	87%	0.0419	76%

high glycerol concentrations, even a small amount of water added to the solution dramatically lowers the viscosity. To check whether this is a plausible explanation, we applied the equation to instead calculate the viscosity of the glycerol solution from the experimentally derived diffusion coefficients. That viscosity was then compared to the reference values[34] at +20 °C to estimate the glycerol concentration. The results are summarized in **Table 2**. The calculated glycerol concentrations are in good agreement with each other, regardless of the FND size.

In case of the 75% glycerol solution, the calculated values are closer to the expected ones, except for the case of 70 nm FNDs. This discrepancy is likely due to the way MSD curves are used to calculate the diffusion coefficients (and, by extension, the parameters of the environment, such as viscosity). As we can see in the MSD curves of, for example, 120 nm particles (Figure 3D), most of the FNDs were confined. However, at low τ values the MSD curves still showed some growth. The diffusion coefficient D was calculated based on the MSD for $\tau = 1$ (i.e., the change in the particle's position between two consecutive positions on the trajectory). Since for the 120 nm particles almost none of the trajectories were completely flat, we could still use these data to estimate the diffusion. These trajectories can be interpreted as particles being confined within a certain volume (= tethered), but exhibiting some Brownian motion that we could detect.

The situation with 70 nm FNDs was different. In this case, a large portion of the MSD curves were flat from the very beginning (Figure 3F), which means that no matter how long we observed the particles, their displacement from the point of origin did not change. Most of the recorded particles were very highly confined/immobilized, at least at the scale of our measurements (spatial and temporal resolution). Using these data for MSD analysis leads to a severe underestimation of the diffusion coefficient and overestimation of the viscosity of the particle's environment. If we select only the non-confined trajectories for the analysis, the resulting diffusion coefficient D3D will be 914×10^{-4} μm^2 s^{-1} (expected value 1109×10^{-4} μm^2 s^{-1}), and the estimated viscosity of the solution will be 0.0671 Pa s (glycerol concentration close to 81%).

It is worth noting that all measurements in 75% glycerol overestimate the viscosity of the solution. As we have discussed earlier, the MSD curve should start with the slope close to 1 to obtain the true diffusion coefficient. If α is less than 1, the resulting diffusion coefficient will be underestimated (and the viscosity—overestimated). However, we see this even in case of 40 nm particles, which exhibit simple diffusion at the beginning of the MSD curve. In this case, the overestimated viscosity might be caused by the setup limitations. Smaller FNDs (38 and 40 nm ones) move very fast in less viscous solutions, and their fluorescence is relatively dim, which makes tracking problematic (hence we were not able to track the 38 nm particles in 75% glycerol). The recorded trajectories might come from small aggregates rather than individual FNDs, since only these would be bright enough and slow enough to be tracked. In this case, using the size of the individual particles would result in overestimated viscosity of the medium.

We then compared the total volume explored by the FNDs of different sizes in 100% glycerol over the same time. The results shown in Figure S19, Supporting Information, are consistent with previous findings: smaller particles diffuse further away from the origin than larger particles.

To summarize, our method has certain limitations when it comes to very precise measurement of the diffusion parameters. Nevertheless, we are able to get information on the mode of motion experienced by the particles. The diffusion coefficients calculated from the MSD curves reflect the size of the particles and the viscosity of the environment. The explored volume can be used as an additional parameter to characterize the particle's fate. We then built upon these results, applying the tracking to FNDs internalized by live HeLa cells.

2.3. FND Trajectories in Live Cells

In most cases, FNDs moving inside HeLa cells showed confined diffusion with additional ballistic movement (compare to Figure S2A, Supporting Information). At 2 h of incubation, the majority of FNDs is expected to be found in the endosomes. The value of MSD at the plateau gives us the estimate of the volume available to the particle (= the size of the endosome). For 120 nm FNDs (**Figure 5**A), the estimated radius of the endosome would be $\approx\sqrt{0.30} = 0.548$ μm, which is consistent with the size of the early endosomes. For 70 nm FNDs (Figure 5C), we can see two subsets of particles that exhibit this kind of behavior (diffusing within a moving confinement). For the lower subset, the estimated radius of the endosome is again $\sqrt{0.30} = 0.548$ μm, whereas the higher subset moves within a larger volume of $\approx\sqrt{0.65} = 0.806$ μm. The higher subset of

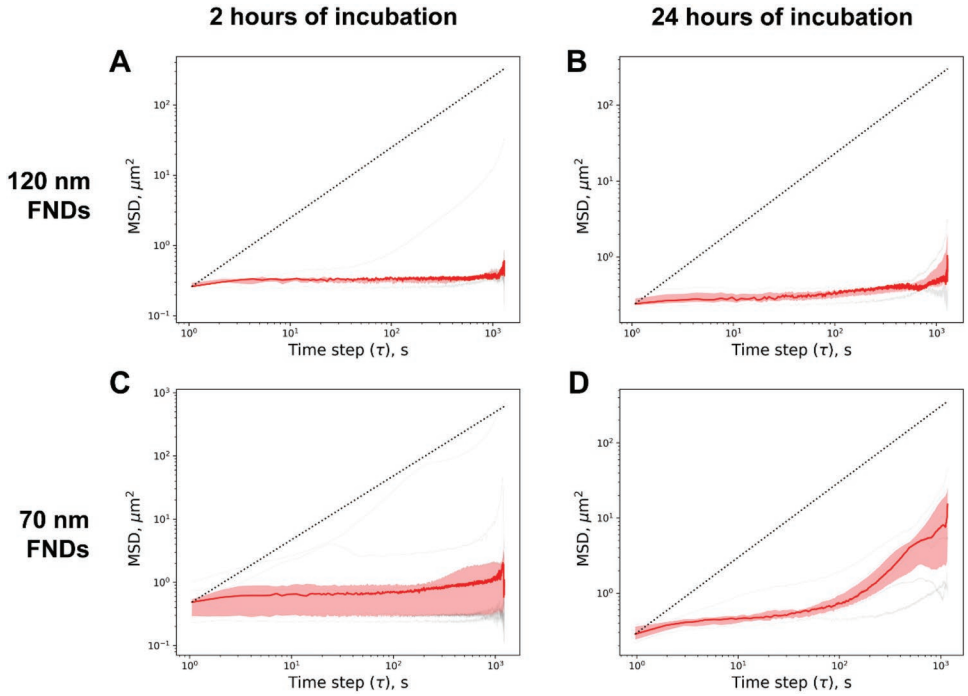

Figure 5. MSD curves of FNDs internalized by HeLa cells at different times of incubation. The trajectories are recorded relative to the setup drift and represent the combination of the particle's movement within the cell and the movement of the cell itself. Each figure shows individual MSDs of trajectories as grey lines and the median of all MSDs under the given conditions is set as a bold red line. The dotted black line depicts a slope of 1, indicating ideal random movement. The shaded red region shows the interquartile range of MSDs. The number of the trajectories shown in each panel is: 5 (A), 3 (B), 9 (C), 6 (D).

particles is also transported further away from the point of origin, and can represent the FNDs inside the endosomes at a later stage of maturation. Interestingly, the one 120 nm FND that is actively transported within the cell over a large distance (Figure 5A, the top grey MSD curve) is also confined within a larger volume—its MSD plateaus at ≈0.45 μm^2, which is equivalent to a vesicle with a radius of $\sqrt{0.45} = 0.671$ μm.

At 24 h, the majority of FNDs should have escaped the endosomes[35] and are expected to diffuse freely in the cytoplasm. While this does not seem to be the case for 120 nm FNDs (Figure 5B), the transition from the diffusion to the plateau in the MSD plots is less clear. Instead, the particles seem to be almost completely immobilized, while being very slowly carried away (the slope of the curve increases at longer τ), possibly due to the movement of the cell itself. If FNDs are, indeed free in the cytoplasm, they might be too large to move through the crowded intracellular environment or become trapped due to some interactions with the cellular components. In contrast, 70 nm FNDs show characteristic bow-like MSD curves, corresponding to a relatively fast movement of the confinement (Figure S2C, Supporting Information). The radius of the confinement is, on average, larger than at 2 h (≈0.707 μm), and the ballistic component (the upward trend at the end of the MSD curves) is way more pronounced. This behavior would be consistent with the particles being actively transported, while trapped inside relatively large late endosomes, rather than diffusing freely in the cytoplasm.

It should be noted that the trajectories are always recorded relative to the setup and represent the combination of the particle's movement within the cell and the movement of the cell itself. At the same time, the cell movement over the course of the short, 20-min experiments is usually limited. An actively migrating HeLa cell on a glass surface moves at ≈12 μm h^{-1}[36] (0.003 μm s^{-1}), resulting in an expected displacement of 4 μm by the end of the experiment. The speed of the endosomal movement, driven by molecular motors, such as kinesins, myosins, and dynein, is ≈1 μm s^{-1}[37]—two orders of magnitude higher than that of the entire cell. The instantaneous speeds of FNDs recorded inside of the cells range from 0.3 to 0.5 μm s^{-1} (Table S3, Supporting Information), additionally pointing to the presence of active intracellular transport.

The total volume explored by the FNDs is shown in **Figure 6**. As expected, FNDs internalized by the cells were much more confined than those moving in glycerol solution. 120 nm FNDs were, in general, less mobile than 70 nm particles. FNDs of both sizes had a larger volume available to them after 24 ho of incubation, as compared to 2 h of incubation.

2.4. FND Trajectories in Live Cells, Combined with Long-Term T1 Monitoring

For the next set of experiments, we chose 120 nm FNDs, as they are easier to follow over the long periods of time and are less likely to be lost. We combined the tracking with the T1 measurements for FNDs that have been incubated with the cells for either 2 or 24 h. The long trajectories were split into 20-min segments to allow for the comparison of the MSD curves and

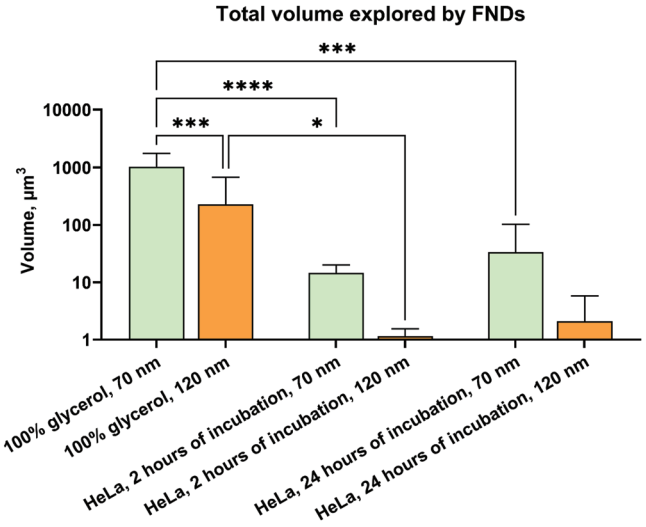

Figure 6. Total volumes explored by FNDs, moving in 100% glycerol or inside the live HeLa cells. The columns represent the median volume, the error bars—25% and 75% percentiles. The number of the analyzed trajectories is: 100% glycerol, 70 nm –37; 100% glycerol, 120 nm –40; HeLa, 2 h of incubation, 70 nm –9; HeLa, 2 h of incubation, 120 nm –5; HeLa, 24 h of incubation, 70 nm –6; HeLa, 24 h of incubation, 120 nm –3. The asterisks indicate the statistical significance of the differences between groups, measured with Kruskal–Wallis test and Dunn's post-hoc multiple comparisons test. *: $p < 0.05$, ***: $p < 0.001$, ****: $p < 0.0001$.

all calculated parameters from these experiments and the previously recorded trajectories in HeLa cells and glycerol.

In the first experimental run (**Figure 7**, 2 h of incubation), the FND was located next to a cell surface and has proven to not be associated with the cell, as is evidenced by bright-field images (Figure 7A,B). Over the course of the experiment (14 h), the particle has not moved much (Figure 7C,D). The MSD curves of the trajectory segments show confined diffusion within a relatively small volume, which is, at the same time, larger than an endosome (the radius is estimated to be 1.3 µm). The T1 values do not change much, which is not unexpected, as the particle does not change its location and is not internalized by a cell. The confinement might be caused by the debris and protein networks present outside the cells or can result from the FND being inside an extracellular vesicle. It has been previously shown that FNDs can be actively exocytosed from the cells.[38] Alternatively, the particle could have been encapsulated in an apoptotic body, coming from one of the cells that have died in the sample prior to the measurement.

In the next run (**Figure 8**, 2 h of incubation), the cell was moving substantially over the course of the experiment. The bright-field images show that the cell of interest has migrated and shrunk, possibly going toward cell death. At the end of the experiment, the setup has jumped to another nanodiamond in a neighboring cell (Figure 8C,D), resulting in a set of new positions and T1 values. The overlay of T1 values and 3D-trajectory shows the complex map of T1, with domains of higher or lower values, which can be interpreted as domains of lower or higher free radical load. This trajectory is substantially affected by the movement of the cell itself, which results in a combination of a spatial and temporal T1 map. A very large size of confinement, derived from the MSD curves (Figure 8E) indicates that the particle might be moving freely in the cytoplasm, as opposed to being confined in an endosome. In this case, the FND might be passing by the intracellular sources of free radicals (e.g., mitochondria), which would cause the change in T1. At the same time, the overall T1 hardly changes over the course of the experiment, emphasizing the need of T1 mapping to make sense out of the results of long-term measurements.

In the last experiment (**Figure 9**, 24 h of incubation), the cell has remained in largely the same position, but the FND has moved substantially through the cytoplasm. As the cell does not migrate much, the overlay of recorded T1 values and 3D trajectory gives a clear map of the T1 values along the course of the track. In this case, the T1 values have substantially decreased over the course of the experiment, which might reflect a higher free radical load in the environment of the FND. Although local radical concentrations are scarcely available, the literature estimates concentrations in the nanomolar to micromolar range.[39,40] Based on previous work under controlled conditions in a chemical environment, we can ascertain that the concentrations we can estimate from T1 measurements are indeed in this expected concentration range.[6,9] This can stem either from the particle arriving at a more radical-rich subcellular location or the cell being stressed and undergoing apoptosis—the bright-field images show that the cell has shrunk during the experiment, and some of the neighboring cells have died as well. Notably, the MSD curves show a larger spread than in experiment 2 (Figure 8E), which might reflect changes in the viscosity of the environment of the FND. Indeed, at the beginning of the experiment, the diffusion coefficient of the FND (in *XY*) is 186×10^{-4} µm^2 s^{-1}, and it increased to 820×10^{-4} µm^2 s^{-1} by the end of the trajectory. Moreover, the particle moved more rapidly during the first part of the experiment, covering 5 µm in 20 min, as opposed to 1.5 µm during the last 20 min of the trajectory. The MSD curves evolve from a combination of rapid ballistic movement and very confined diffusion to diffusion in a slowly moving confinement with a radius of 0.55 µm to confined diffusion in a container with a radius of 2 µm (Figure S20, Supporting Information). These events (and the corresponding changes in T1s) might reflect the endosomal escape of the FND, rather than apoptosis, as cell death would have caused increase in the cytoplasm viscosity,[41] not the decrease that we observe here.

To summarize, in a live cell FNDs exhibit complex movement patterns, resulting from the combination of their own random diffusion, the confinement of the intracellular vesicles and other cellular structures, the ballistic movement of the endosomes, being transported by the molecular motors, the flow of the cytoplasm, and the movement of the cell itself. These processes can be made visible via the analysis of the trajectories of the particles, the corresponding MSD curves, and the other attributes, such as the diffusion coefficient, the particle's total displacement, and the total explored volume. As we show, this can provide the much-needed intracellular context for the measurements performed with FNDs (such as T1 relaxometry) in real time, in parallel with the main experiment, without additional staining of the intracellular structures.

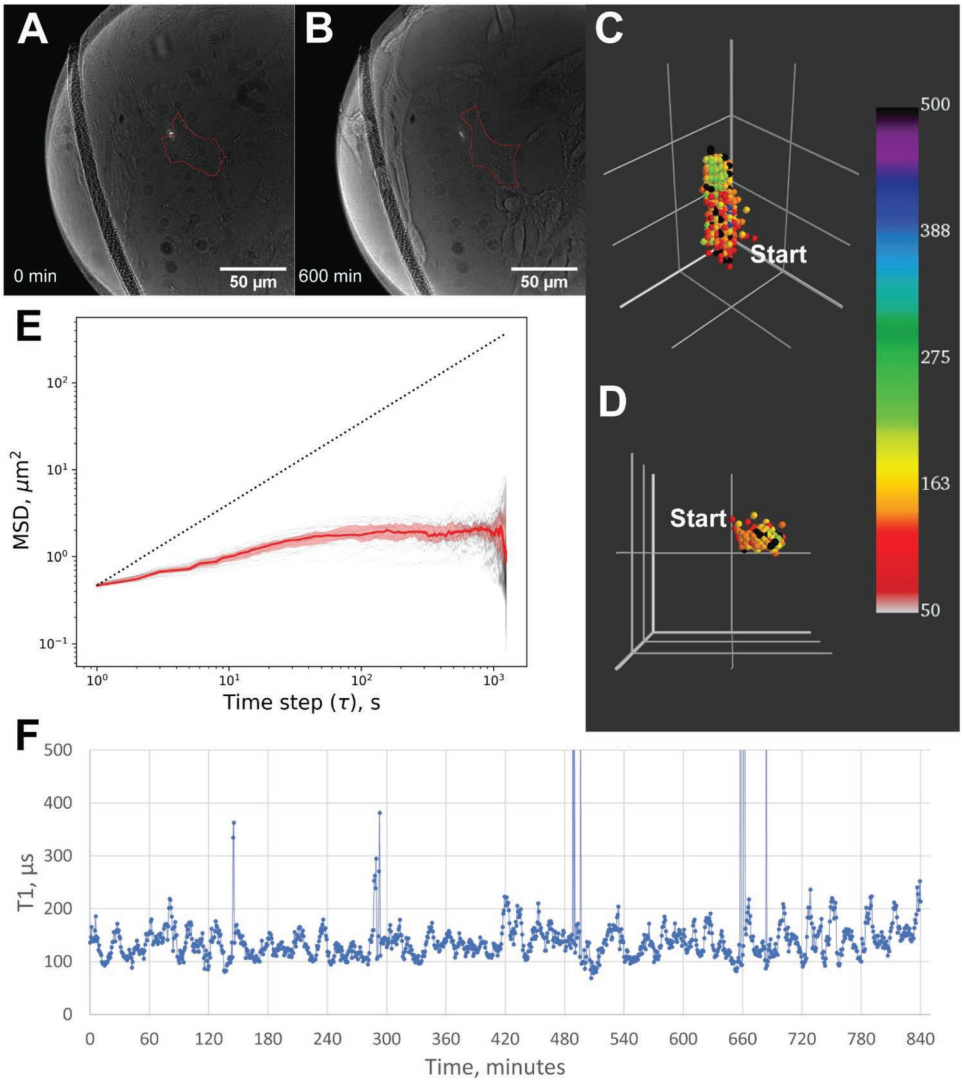

Figure 7. The observed FND was outside of the cell after 2 h of pre-incubation and remained roughly at the same position throughout the experiment. A,B) Bright-field images show the location of the laser beam, focused on the FND, as well as the cells in the sample. The red markers show the border of the cell of interest, as manually segmented from the bright-field image. C,D) 3D trajectories (C: isometric view, D: top-down view) reveal that the particle has moved within a small volume. The color bar shows T1 in microseconds at the respective positions. Size of the grid is 5 µm. E) MSD curves of 20-min segments of the whole trajectory show confined diffusion throughout the entire experiment. The radius of confinement is estimated at 1.3 µm for each of the segments. F) T1 fluctuates around the average value of 142 µs over the course of the experiment, without substantial changes over time (linear fit equation: $Y = 0.0366x + 126.57$; $R^2 = 0.0136$).

3. Conclusion

Single-particle trajectory analysis is a valuable and rich source of information on the immediate environment of FNDs. The trajectories and corresponding MSD curves are sensitive to the particle's mode of motion, degree of confinement, shape, and size of confinement, even when those parameters are changing over the course of the trajectory. In this study, we simulated a range of scenarios and analyzed the resulting trajectories to provide handholds for the analysis of experimentally recorded movement of particles.

As we demonstrate here, trajectory analysis can be performed, even if the trajectories are recorded at a relatively low frequency (≈1 Hz). We can differentiate between differently sized FNDs in a way that is more reliable than assessing the fluorescence intensity or the visible size of the particles. This can be helpful if one wants to use FNDs of varying sizes within the same experiment, or if the particle's size is important for the experimental applications.

This approach can be extended to the FNDs internalized by the live cells. We can learn more about the behavior and localization of the FND inside the cell, which gives the background information for the measurements and improves the interpretation of the results.

Finally, trajectory analysis can be combined with the highly spatially accurate T1 measurements in live cells at ambient conditions. Bringing context to the recorded T1 values is essential to make better use of the high sensitivity and spatial resolution of nanodiamond magnetometry, and single-particle tracking can shed light on the intracellular environment of FNDs.

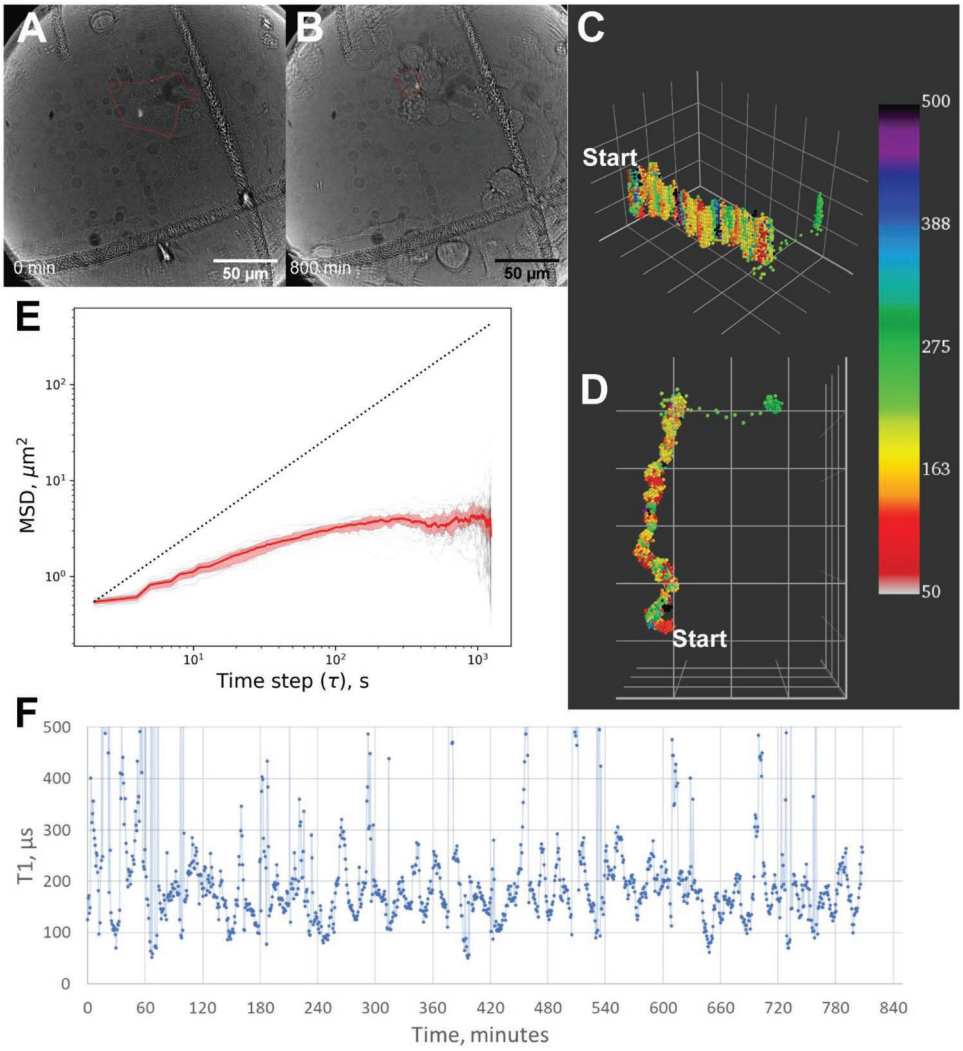

Figure 8. The observed FND was internalized by the cell, which had migrated over the course of the experiment and started rounding up by the end of the acquisition time. Pre-incubation time was 2 h. A,B) Bright-field images show the location of the laser beam, focused on the FND, as well as the cells in the sample. The red markers show the border of the cell of interest, as manually segmented from the bright-field image. C,D) 3D trajectories (C: isometric view, D: top-down view) reveal that the particle has moved substantially, while being confined within a certain volume. At the end of the experiment, the setup jumps to an FND in the neighboring cell. Color bar shows T1 in microseconds at the respective positions. Size of the grid is 5 µm. E) MSD curves of the sub-trajectories show confined diffusion with the confinement radius of 1.9 µm. F) T1 fluctuates around the average value of 206 µs over the course of the experiment, without substantial changes over time (linear fit equation: $Y = -0.0486x + 225.38$; $R^2 = 0.0102$).

4. Experimental Section

Computer Simulations of Different Types of Movement: Particle trajectories were simulated by cumulating steps with independently chosen random step size of 0, 0.3, 0.5, and 1 a.u. in either direction (*X*, *Y*, *Z*), averaging to a velocity of about 0.52 for the randomly moving particles and to 0.88 for the particles with a combination of random walk and ballistic motion.

The following scenarios were programmed:

- *Random walks*
  Trajectories were generated by simulating 1200 steps for each of the three dimensions. For each step, the step size (0, 0.3, 0.5, and 1 a.u.) and the direction (+/−) were randomly chosen. Subsequent steps were added up to calculate the displacement. By following the position along each step of the displacement, the entire trajectory was built.
- *Ballistic movement*
  Ballistic trajectories were generated, using a persistent velocity of (0.05, 0.07, 0.02) a.u. along *X*, *Y*, and *Z* axis, respectively. No random movement was present in this case.
- *Confined diffusion*
  To simulate particles moving within a confined space, first the dimensions of the confinement were defined (e.g., 1.2 by 1.2 by 1.2 a.u.). Whenever the simulated particle would be crossing the boundaries, it instead was stopped and reflected back inside the volume of the confinement.
- *Combination*
  To simulate the complex processes that could occur within the confined space of an actively moved endosome, all the abovementioned scenarios were combined. As an example, the particle would be in a confined space that would itself be moving

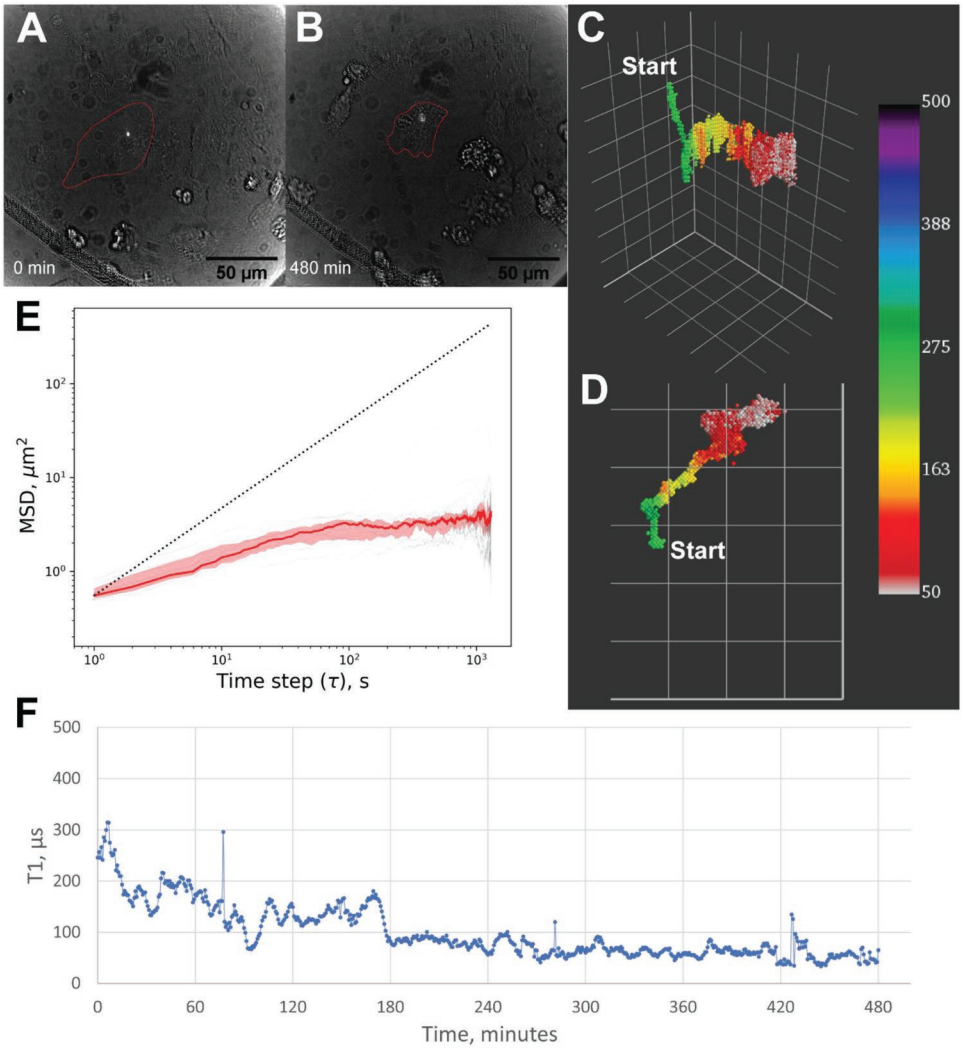

Figure 9. The observed FND was internalized by the cell, which has not migrated over the course of the experiment. Pre-incubation time was 24 h. A,B) Bright-field images show the location of the laser beam, focused on the FND, as well as the cells in the sample. The cell of interest (red outline) has become less spread by the end of the acquisition time. The red markers show the border of the cell of interest, as manually segmented from the bright-field image. C,D) 3D trajectories (C: isometric view, D: top-down view) show that the particle has moved substantially, while being confined within a certain volume. The color bar shows T1 in microseconds at the respective positions. Size of the grid is 5 µm. E) MSD curves of the sub-trajectories show confined diffusion with a slight ballistic component. The radius of the confinement is estimated at 1.7 µm. F) T1 starts with the value of 246 µs and decreases over the course of the experiment, reaching the average value of 53 µs by the last 30 min (linear fit equation: $Y = -0.3173x + 176.02$; $R^2 = 0.6896$).

ballistically (i.e., with each step, the boundaries of the confinement would be shifted).

All simulations were performed in Python 3.10.

Trajectory Analysis: To analyze the trajectory, the datasets (recorded in the four dimensions of time [t] and X, Y, and Z coordinates) were treated according to the following workflow. The starting time was subtracted from all subsequent time entries, to obtain the time elapsed since the start of the trajectory. To better visualize the trajectory it was plotted in 3D as well as in all 2D planes (XY, XZ, and YZ). The MSDs were calculated as the averaged displacement of the FNDs according to $MSD(\tau)$ $\langle r^2(\tau)\rangle$ $(r(t+\tau) - r(t))^2\rangle$ with r being the position of the particle and τ as the time step. These MSDs were plotted in a log–log scale versus the amount of time that had elapsed between the respective start and end of each sub trajectory (again τ). For the 3D trajectories, the time dependency of the MSD was given as $r(t)^2 > 6Dt^{\alpha}$, with D being the diffusion coefficient of the FND in the current medium, and α the scaling exponent. Note, that D depended on the viscosity, and hence could change within the cellular confinement in which the experiments took place. Note furthermore that α gave a strong indication of the trajectory. $\alpha = 1$ was true for random motion, a higher α stemmed from ballistic motion, and a plateau in the MSD ($\alpha = 0$) meant that a particle was confined and had explored all the volume of its confinement. The ordinate of such an MSD could be used to calculate the size of the confinement.

The α, appearing in the exponent, would be later on the slope, as the MSDs were plotted in a log–log graph, as by using the logarithm, exponents became factors. The plots of MSDs all showed an $\alpha = 1$ as black dotted line for internal reference, as a slope of one denoted perfect random motion.

From the MSDs, the diffusion coefficient D in both 3D and for all the 2D-planes was also calculated. Additionally, the total displacement of the

particles (squared distance between the origin and the end point of the trajectory) and the total volume explored by the particle were analyzed. The volume was estimated as a bounding box of the trajectory—that is, the product of the maximal distances the particle had travelled in each of the three dimensions.

Nanodiamonds: FNDs were purchased from Adamas Nanotechnologies as pre-made solutions in deionized water (1 mg mL^{-1}). The sizes of the particles, according to the manufacturer, had distributions with the modal values of 40, 70, 120, or 140 nm (as measured by the manufacturer with dynamic light scattering on a Malvern Zetasizer Nano ZS [Malvern Instruments, Ltd., UK]).

The "round" FNDs were produced by a previously described technique[35,42] based on kinetically controlled etching of diamond vertexes and edges by molten KNO_3.[43] CAUTION! Although the procedure had been safely reproduced many times, it involved heating of a carbon nanomaterial in a hot strongly oxidizing reagent, which could lead potentially to a risk of fire or explosion. All safety and personal protection must be carefully secured! Briefly, 0.5 g of high pressure/high temperature nanodiamonds (NDs) (Microdiamant, MSY 0–0.1) were mixed with 25 g of KNO_3 and homogenized in a glass mortar. The obtained fine powder was transferred into reaction vessel preheated to 565 °C, which contained 75 g of molten KNO_3. The mixture was kept in the furnace for 8 min. The reaction was terminated by pouring the molten mixture into 300 mL of cold water. The suspension was centrifuged and the round NDs were oxidized in stirred mixture of HF and HNO_3 (2:1 v/v, 45 mL; 48 h at 160 °C) in 60 mL perfluoroalkoxy copolymer (PFA) vessel (Savillex). Oxidized round NDs were centrifuged, washed with Milli-Q water, NaOH (1 M), HCl (1 M), five times with Milli-Q water, and freeze-dried.

The round NDs were irradiated with a proton beam extracted from the isochronous cyclotron U-120 M (4.5 h, 15.4 MeV, 1.55×10^{18} p^+/2 mL) in the form of colloidal 5% aqueous solution ensuring a homogeneous irradiation.[44] The irradiated NDs were annealed in Ar atmosphere (900 °C, 1 h), air oxidized (510 °C, 4 h and 40 min), and finally oxidized in a stirred mixture of H_2SO_4, $HClO_4$, and HNO_3 (fuming) (1:1:1, v/v/v, 18 mL; 48 h at 90 °C) in 45 mL PFA vessel followed by washing as described above. The round FNDs were stored as 1 mg mL^{-1} solution in deionized water. The round FNDs showed particle circularity 0.758 and number-weighted mean diameter 38 nm (see Figure S21, Supporting Information, for transmission electron microscopy and size distribution analysis[45]).

Drift Correction: One of the sources of error, when estimating the movement of particles, was the drift of the microscope. To check whether the setups exhibited this behavior, the nanodiamond trajectories in dry samples were recorded. Several small droplets of the 120 nm FND stock solution were placed on the bottom of the glass bottom Petri dish and waited for the solvent to completely evaporate.

The nanodiamond trajectories were recorded using a home-made confocal microscope, as described previously.[46] First, an individual FND would be selected from the single-plane image of the sample, based on stable, non-bleaching fluorescence, with at least 1 000 000 photon counts per second. The coordinates of the particle were saved by the software. After the particle had been manually selected, the software took a 2×2 µm image of a single optical plane. Based on the Gaussian fitting of the *XY* intensity profiles of the resulting image, the software calculated the position of the particle's center. Then a 2-µm *Z*-stack of the center was acquired to determine the *Z*-axis position of the nanodiamond center. The calculated *XYZ* coordinates of the center were recorded, and the procedure was repeated 1250 times, continuously recording the positions of the nanodiamond for 20 min, with each repetition taking ≈1 s.

To check whether there was a consistent drift, the average displacement of the tracked particles from the point of origin over the course of the experiment along each individual axis was calculated. The resulting "displacement versus time" curves were fitted with a linear equation and the slope was used as the measure of drift. This drift was subtracted from the coordinates of the particles moving in glycerol solutions or in cells, and corrected trajectories were used for further analysis.

A wide-field timelapse series of a larger area of the sample (20×20 µm, 200×200 pixels) was also recorded. The acquisition time was 45 s, and the images were taken every minute for a total of 20 min. The resulting timed series was processed in FIJI, using the "Hyperstacks → Temporal color-code" function to obtain a color-coded image, showing the overlayed positions of the particles in the field of view, as they changed during the experiment.

This procedure was repeated for both setups used in this study. The first setup, which lacked the T1 pulsing functionality, was used to record the trajectories of FNDs moving in glycerol or in live cells (Sections 2.2 and 2.3 of the Results). The second setup allowed to record the FND trajectory in parallel with performing T1 measurements and was only used for the experiments where T1 values were obtained (Section 2.4 of the Results).

Recording Nanodiamond Trajectories in Glycerol Solutions: To assess the behavior of nanodiamonds in a less complex environment, the FND suspensions were prepared in either 100% or 75% glycerol (in water, by weight). The stock solution of FNDs was added directly to the glycerol solution to reach the final concentration of 3 µg mL^{-1}. The resulting suspension was carefully pipetted to mix FNDs with glycerol, while not forming air bubbles, and transferred to a 35 mm glass bottom Petri dish. The dish was sealed with parafilm to minimize the exchange between the suspension and the atmosphere, and immediately used for imaging. The experiments were performed at room temperature (+20 °C). The nanodiamond trajectories were recorded, as described in the previous section.

Cell Culture: HeLa cells were routinely cultured in complete DMEM-HG medium (10% fetal bovine serum [FBS], 1% penicillin/streptomycin) at +37 °C, 5% CO_2. Prior to the experiment, the cells were seeded in a quartered glass bottom Petri dish and allowed to recover for 24 h.

Recording Nanodiamond Trajectories in Live Cells: On the day of the experiment, FNDs were added to the cells. As the cells had a certain level of background autofluorescence, only the relatively large and bright FNDs were used for these experiments (70 and 120 nm). For FND internalization, the FND stock solution was pre-mixed with FBS to prevent FND aggregation. Then the mix was dissolved in the serum-free cell culture medium to reach the desired concentration of 1 µg mL^{-1}. The cell culture medium in the Petri dishes with cells was replaced with FND solution, and the cells were incubated for 2 or 24 h at +37 °C.

When the incubation was over, the trajectories of FNDs internalized by the cells were recorded, as described previously. The FNDs were selected from the single-plane confocal image of the cells. As the focused laser beam could be seen in the bright-field image, collected with a camera from the same field of view, one could use it to verify that the selected particle was located within the cell boundaries. Each trajectory contained 1250 steps and spanned ≈20 min.

Recording T1 Maps in Live Cells: To perform a long-term measurement of T1, combined with the trajectory of FND inside a live cell, the solution of 120 nm FNDs and a Petri dish with HeLa cells were prepared, as described previously. For these experiments, non-quartered dishes with gridded glass bottom (Ibidi) were used to allow for the bright-field imaging and identification of the cell of interest. These dishes also had a lid lock, which reduces the water evaporation from the dish. The microscope stage was heated to +37 °C by a feedback-controlled heating element.

The nanodiamond solution was added to the cells, and the sample was immediately brought to the experimental setup. Using the confocal mode and a bright-field camera, it was found that an FND was internalized by a HeLa cell. This FND was then used to continuously record T1 values of the NV-center relaxation while it moved inside the cell.

The procedure for T1 measurements and analysis was described in a previous work.[8] Briefly, a laser pulsing sequence was used to initialize and readout the NV-center's spin state. A train of 50 pulses lasting 5 µs each was generated by an Acousto-Optic Modulator (Gooch & Housego AOMO 3350-199 [160 ns rise/fall time]) in a double-pass configuration and routed to the FNDs. The initial TTL pulses were created by a pulse

generator (PulseBlasterESR-PRO 500, SpinCore Technologies) and directly sent to the AOM Driver (1350AFP-D-1.0, Gooch & Housego). The 49 dark-time τ (delay between the pulses) were logarithmically swept from 0.2 µs to 10 ms, and the photoluminescence was collected after each dark time. Such a dark-time sweep was repeated a total of 6 000 000 times per experiment. The whole dataset was then analyzed using the rolling window approach. The photoluminescence of first 10 000 sweeps was summed to obtain the photoluminescent pulses. The photoluminescence signal (PL(τ)) during the first 1 µs of each pulse after different dark times τ was then integrated. PL(τ) was then plotted and the resulting relaxation curve was fitted by two exponential functions for extracting T1.[6] The procedure was then repeated by shifting the summation window by 2000 sweeps to ultimately obtain the T1 versus time curves.

In parallel with T1 measurements, the position of the particle was recorded every 1 s, using the tracking algorithm described previously. A bright-field image of the fixed field of view, including the cell of interest, was automatically taken every 15 min to assess the general morphology of the cell and, if possible, the position of the laser beam tracking the FND with respect to the cell borders and nucleus. The whole experiment spanned 14 h, comprising 6 million repetitions of the T1 laser pulsing sequence and 50 400 positions of the FND along its trajectory.

Statistical Analysis: The raw data were processed as described in the "Trajectory analysis" section to extract the MSD curves, diffusion coefficients, total displacement, and total volume explored by the particles. The results were presented as either median values ± interquartile range or mean values ± standard deviation, as indicated in the figure and table captions. The sample size for each dataset can be found in the captions of corresponding figures.

The level of statistical significance of the differences between the groups was assessed with Kruskal–Wallis test, followed by Dunn's post-hoc multiple comparisons test, unless otherwise indicated. *p*-value of 0.05 was chosen as the threshold for statistical significance. *p*-values of 0.05 and higher were not shown in the plots. Multiplicity adjusted *p*-values were reported in the figures as follows:

- * – $p < 0.05$
- ** – $p < 0.01$
- *** – $p < 0.001$
- **** – $p < 0.0001$

Supporting Information

Supporting Information is available from the Wiley Online Library or from the author.

Acknowledgements

A.S. and A.H. contributed equally to this work. The authors are grateful to Dr. Jan Stursa for irradiation of nanodiamonds, to Dr. H. Raabova and Dr. J. Schimer for technical support in rounding of nanodiamonds, and to M. Kindermann for help with image analysis of TEM data. This work was financially supported by an ERC starting grant, (ERC-2016-STG Stress Imaging 714289). The work was further supported by the European Regional Development Fund, OP RDE, Project: CARAT (No. CZ.02.1.01/0.0/0.0/16_026/0008382) (to P.C. and M.S.). Irradiation was supported through MSMT project No. LM2015056 within the CANAM infrastructure of the NPI CAS Rez.

Conflict of Interest

The authors declare no conflict of interest.

Data Availability Statement

The data that support the findings of this study are available in the supplementary material of this article.

Keywords

fluorescent nanodiamonds, free radicals, magnetometry, single-particle tracking

Received: March 3, 2022
Revised: July 26, 2022
Published online:

[1] N. J. McLaughlin, H. Wang, M. Huang, E. Lee-Wong, L. Hu, H. Lu, G. Q. Yan, G. Gu, C. Wu, Y. Z. You, C. R. Du, *Nano Lett.* **2021**, *21*, 7277.
[2] L. Thiel, Z. Wang, M. A. Tschudin, D. Rohner, I. Gutiérrez-Lezama, N. Ubrig, M. Gibertini, E. Giannini, A. F. Morpurgo, P. Maletinsky, *Science* **2019**, *364*, 973.
[3] Y. Dovzhenko, F. Casola, S. Schlotter, T. X. Zhou, F. Büttner, R. L. Walsworth, G. S. D. Beach, A. Yacoby, *Nat. Commun.* **2018**, *9*, 2712.
[4] T. Rendler, J. Neburkova, O. Zemek, J. Kotek, A. Zappe, Z. Chu, P. Cigler, J. Wrachtrup, *Nat. Commun.* **2017**, *8*, 14701.
[5] J. Barton, M. Gulka, J. Tarabek, Y. Mindarava, Z. Wang, J. Schimer, H. Raabova, J. Bednar, M. B. Plenio, F. Jelezko, M. Nesladek, P. Cigler, *ACS Nano* **2020**, *14*, 12938.
[6] F. P. Martínez, A. C. Nusantara, M. Chipaux, S. K. Padamati, R. Schirhagl, *ACS Sens.* **2020**, *5*, 3862.
[7] M. Karadas, A. M. Wojciechowski, A. Huck, N. O. Dalby, U. L. Andersen, A. Thielscher, *Sci. Rep.* **2018**, *8*, 4503.
[8] L. Nie, A. C. Nusantara, V. G. Damle, R. Sharmin, E. P. P. Evans, S. R. Hemelaar, K. J. van der Laan, R. Li, F. P. P. Martinez, T. Vedelaar, M. Chipaux, R. Schirhagl, *Sci. Adv.* **2021**, *7*, eabf0573.
[9] R. Sharmin, T. Hamoh, A. Sigaeva, A. Mzyk, V. G. Damle, A. Morita, T. Vedelaar, R. Schirhagl, *ACS Sens.* **2021**, *6*, 4349.
[10] K. van der Laan, M. Hasani, T. Zheng, R. Schirhagl, *Small* **2018**, *14*, 1703838.
[11] Y. Y. Hui, W. W. W. Hsiao, S. Haziza, M. Simonneau, F. Treussart, H. C. Chang, *Curr. Opin. Solid State Mater. Sci.* **2017**, *21*, 35.
[12] D. A. Simpson, A. J. Thompson, M. Kowarsky, N. F. Zeeshan, M. S. J. Barson, L. T. Hall, Y. Yan, S. Kaufmann, B. C. Johnson, T. Ohshima, F. Caruso, R. E. Scholten, R. B. Saint, M. J. Murray, L. C. L. Hollenberg, *Biomed. Opt. Express* **2014**, *5*, 1250.
[13] W. Liu, F. Yu, J. Yang, B. Xiang, P. Xiao, L. Wang, *Adv. Funct. Mater.* **2016**, *26*, 365.
[14] S. Haziza, N. Mohan, Y. Loe-Mie, A. M. Lepagnol-Bestel, S. Massou, M. P. Adam, X. L. Le, J. Viard, C. Plancon, R. Daudin, P. Koebel, E. Dorard, C. Rose, F. J. Hsieh, C. C. Wu, B. Potier, Y. Herault, C. Sala, A. Corvin, B. Allinquant, H. C. Chang, F. Treussart, M. Simonneau, *Nat. Nanotechnol.* **2017**, *12*, 322.
[15] Y. Wu, S. Cao, M. N. A. Alam, M. Raabe, S. Michel-Souzy, Z. Wang, M. Wagner, A. Ermakova, J. J. L. M. Cornelissen, T. Weil, *J. Mater. Chem. B* **2021**, *9*, 5621.
[16] P. Moscariello, M. Raabe, W. Liu, S. Bernhardt, H. Qi, U. Kaiser, Y. Wu, T. Weil, H. J. Luhmann, J. Hedrich, *Small* **2019**, *15*, 1902992.
[17] F. J. Hsieh, S. Sotoma, H. H. Lin, C. Y. Cheng, T. Y. Yu, C. L. Hsieh, C. H. Lin, H. C. Chang, *ACS Appl. Mater. Interfaces* **2019**, *11*, 19774.
[18] S. Sotoma, J. Iimura, R. Igarashi, K. M. Hirosawa, H. Ohnishi, S. Mizukami, K. Kikuchi, T. K. Fujiwara, M. Shirakawa, H. Tochio, *Nanomaterials* **2016**, *6*, 56.

[19] C. P. Epperla, N. Mohan, C. W. Chang, C. C. Chen, H. C. Chang, *Small* **2015**, *11*, 6097.
[20] B. Zhang, Y. Li, C. Y. Fang, C. C. Chang, C. S. Chen, Y. Y. Chen, H. C. Chang, *Small* **2009**, *5*, 2716.
[21] Y. R. Chang, H. Y. Lee, K. Chen, C. C. Chang, D. S. Tsai, C. C. Fu, T. S. Lim, Y. K. Tzeng, C. Y. Fang, C. C. Han, H. C. Chang, W. Fann, *Nat. Nanotechnol.* **2008**, *3*, 284.
[22] C. C. Fu, H. Y. Lee, K. Chen, T. S. Lim, H. Y. Wu, P. K. Lin, P. K. Wei, P. H. Tsao, H. C. Chang, W. Fann, *Proc. Natl. Acad. Sci. U. S. A.* **2007**, *104*, 727.
[23] T. Savin, P. S. Doyle, *Biophys. J.* **2005**, *88*, 623.
[24] X. Michalet, *Phys. Rev. E: Stat., Nonlinear, Soft Matter Phys.* **2010**, *82*, 041914.
[25] R. Metzler, J. H. Jeon, A. G. Cherstvy, E. Barkai, *Phys. Chem. Chem. Phys.* **2014**, *16*, 24128.
[26] E. Kepten, A. Weron, G. Sikora, K. Burnecki, Y. Garini, *PLoS One* **2015**, *10*, e0117722.
[27] S. C. Weber, M. A. Thompson, W. E. Moerner, A. J. Spakowitz, J. A. Theriot, *Biophys. J.* **2012**, *102*, 2443.
[28] M. P. Backlund, R. Joyner, W. E. Moerner, *Phys. Rev. E: Stat., Nonlinear, Soft Matter Phys.* **2015**, *91*, 062716.
[29] I. Medina, J. Deuerling, P. Kumari, S. Scholl, M. Rädle, *Micromachines* **2021**, *12*, 940.
[30] Y. Hayashi, A. Puzenko, I. Balin, Y. E. Ryabov, Y. Feldman, *J. Phys. Chem. B* **2005**, *109*, 9174.
[31] H. Nakagawa, T. Oyama, *Front. Chem.* **2019**, *7*, 731.
[32] J. Bachler, V. Fuentes-Landete, D. A. Jahn, J. Wong, N. Giovambattista, T. Loerting, *Phys. Chem. Chem. Phys.* **2016**, *18*, 11058.
[33] H. Zheng, S. A. Claridge, A. M. Minor, A. P. Alivisatos, U. Dahmen, *Nano Lett.* **2009**, *9*, 2460.
[34] A. Volk, C. J. Kähler, *Exp. Fluids* **2018**, *59*, 75.
[35] Z. Chu, S. Zhang, B. Zhang, C. Zhang, C. Y. Fang, I. Rehor, P. Cigler, H. C. Chang, G. Lin, R. Liu, Q. Li, *Sci. Rep.* **2014**, *4*, 4495.
[36] S. Kauanova, A. Urazbayev, I. Vorobjev, *Front. Cell Dev. Biol.* **2021**, *9*, 391.
[37] E. Granger, G. McNee, V. Allan, P. Woodman, *Semin. Cell Dev. Biol.* **2014**, *31*, 20.
[38] C. Y. Fang, V. Vaijayanthimala, C. A. Cheng, S. H. Yeh, C. F. Chang, C. L. Li, H. C. Chang, *Small* **2011**, *7*, 3363.
[39] B. Halliwell, *Lancet* **1994**, *344*, 721.
[40] L. M. Paardekooper, I. Dingjan, P. T. A. Linders, A. H. J. Staal, S. M. Cristescu, W. C. E. P. Verberk, G. van den Bogaart, *Front. Immunol.* **2019**, *10*, 1216.
[41] F. Liu, J. Wen, S. S. Chen, S. Sun, *Chem. Commun.* **2018**, *54*, 1371.
[42] B. Zhang, X. Feng, H. Yin, Z. Ge, Y. Wang, Z. Chu, H. Raabova, J. Vavra, P. Cigler, R. Liu, Y. Wang, Q. Li, *Sci. Rep.* **2017**, *7*, 46462.
[43] J. Havlik, V. Petrakova, I. Rehor, V. Petrak, M. Gulka, J. Stursa, J. Kucka, J. Ralis, T. Rendler, S. Y. Lee, R. Reuter, J. Wrachtrup, M. Ledvina, M. Nesladek, P. Cigler, *Nanoscale* **2013**, *5*, 3208.
[44] J. Stursa, J. Havlik, V. Petrakova, M. Gulka, J. Ralis, V. Zach, Z. Pulec, V. Stepan, S. A. Zargaleh, M. Ledvina, M. Nesladek, F. Treussart, P. Cigler, *Carbon* **2016**, *96*, 812.
[45] I. Rehor, P. Cigler, *Diamond Relat. Mater.* **2014**, *46*, 21.
[46] A. Morita, T. Hamoh, F. P. P. Martinez, M. Chipaux, A. Sigaeva, C. Mignon, K. J. van der Laan, A. Hochstetter, R. Schirhagl, *Nanomaterials* **2020**, *10*, 516.